Analysis of the Amplitude Response of a Two-Point and a Multi-Point Focused Laser Differential Interferometer

Brett F. Bathel[*], Joshua M. Weisberger[†], Gregory C. Herring[‡]
NASA Langley Research Center, Hampton, VA, 23681

Rangesh Jagannathan[§], Craig T. Johansen[¶]
University of Calgary, Calgary, Alberta, T2N 1N4, Canada

Stephen B. Jones[‖] and Angelo A. Cavone[**]
Analytical Mechanics Associates, Inc., Hampton, VA, 23681

Experiments were performed with two different focused laser differential interferometer (FLDI) instruments to assess the relative amplitude response of each instrument to a traveling shockwave generated by a laser spark in air. The first FLDI instrument generated two slightly-separated measurement points, with each measurement point providing sensitivity to density fluctuations induced by the shockwave. By performing a cross-correlation between the signals obtained from each measurement point, the phase velocity of density fluctuations can be obtained. The second FLDI instrument generated a measurement line that was oriented parallel to the shockwave direction of travel with the resulting interference pattern sampled at multiple equally-spaced points along the line. As a result, this instrument provides density fluctuation measurement capability at multiple points simultaneously. When the measurement line is oriented parallel to the shockwave direction of travel, the phase velocity, rate of change of the phase velocity, and acceleration of density fluctuations traveling along each line can be obtained by performing a cross-correlation between points along the line. Numerical computations of the shockwave generated by the laser spark are used to simulate the response of each instrument and are compared to the experimental results. High-speed schlieren imaging has also been performed and is compared with the FLDI measurements and computational results.

I. Nomenclature

CFD	=	computational fluid dynamics
FLDI	=	focused laser differential interferometer
C_p	=	specific heat at constant pressure [kJ/(kg·K)]
C_v	=	specific heat at constant volume [kJ/(kg·K)]
DS	=	downstream Wollaston pair signal for two-point FLDI system
ε	=	fraction of laser energy used to generate shockwave flow
E	=	laser energy [mJ]
h_{CH}	=	multi-point photodiode element height [mm]
λ_0	=	laser wavelength [nm]
μ	=	viscosity [Pa·s]
M_s	=	shockwave Mach number
N	=	number of radial grid points
N_e	=	number of elements on linear photodiode array

[*]Aerospace Technologist, Advanced Measurements & Data Systems Branch, Mail Stop 493, Senior Member AIAA.
[†]Aerospace Technologist, Advanced Measurements & Data Systems Branch, Mail Stop 493, Member AIAA.
[‡]Aerospace Technologist, Advanced Measurements & Data Systems Branch, Mail Stop 493.
[§]Currently Postdoctoral Research Assistant, University of Oxford, Department of Engineering Science, Parks Road, Oxford, UK, OX13PJ
[¶]Associate Professor, Department of Mechanical & Manufacturing Engineering, 2500 University Drive NW, Senior Member AIAA.
[‖]Research Technician, Advanced Measurements & Data Systems Branch, Mail Stop 493.
[**]Research Technician, Advanced Measurements & Data Systems Branch, Mail Stop 493.

p	=	pressure [Pa]
ρ	=	density [kg/m^3]
r_0	=	spark radius [μm]
r_c	=	cut radius [μm]
r_e	=	extent of computation domain [mm]
r_k	=	radial grid point locations in two-point FLDI simulation
$\delta\theta$	=	azimuthal grid point spacing in two-point FLDI simulation [rad]
T	=	temperature [K]
w_0	=	laser beam waist radius at focus [μm]
$w_{\mathrm{major},0}$	=	laser line major axis waist radius at focus [μm]
$w_{\mathrm{minor},0}$	=	laser line minor axis waist radius at focus [μm]
ΔL	=	laser line total length [μm]
Δx_{NP}	=	Nomarski pair separation [μm]
Δx_{WP}	=	Wollaston pair separation [μm]
$\tilde{x}$	=	multi-point line major axis [μm]
U_{shock}	=	shockwave velocity [m/s]
US	=	upstream Wollaston pair signal for two-point FLDI system
V	=	photodiode element height projected on measurement plane [μm]
$\tilde{y}$	=	multi-point line minor axis [μm]

II. Introduction

THE focusing laser differential interferometer (FLDI) originally described by Smeets and George [1] is capable of providing time-resolved measurements of density fluctuations at a point. The development of high-speed data acquisition systems in recent decades has allowed for the application of this instrument to high-speed supersonic and hypersonic flows [2–17]. Schmidt and Shepherd [18] were the first to develop a numerical method to simulate the response of the FLDI instrument based in part on the theory developed by Fulghum [6] (later summarized in [11]). In their simulations, an idealized sinusoidal disturbance field extending along the instrument's optical axis was used as an input to the simulation and the simulated frequency response compared against theory. Experiments with a steady laminar Argon jet were then performed and the measured phase difference compared against the simulated phase difference of the instrument using a computational fluid dynamics (CFD) solution of the flow as an input. The dynamic response of the instrument to a traveling density disturbance over a cone model in a hypersonic flow was also simulated in [18] and compared against theory. In each of these simulated flows, the contribution of density gradient flow structures away from the instrument's focus to the output signal were assumed negligible (in the case of the Argon jet and traveling disturbance) or could be described by a relatively simple 1-dimensional disturbance integrated along the instrument's optical axis through the measurement volume. In many situations, flow structures away from the FLDI instrument's focus cannot be neglected, are 3-dimensional in nature, and vary non-uniformly in amplitude, frequency, and phase velocity along the instrument's optical axis. Additionally, the flow structure being studied at the focus of the instrument may share characteristics with flow structures away from the focus, complicating interpretation of the FLDI signal.

The purpose of this paper is to simulate the amplitude response for two FLDI instrument configurations borrowing heavily from methods developed by Schmidt and Shepherd in [18] and determine how the response is affected by signal away from the simulated instrument's focus. Here, a traveling shockwave generated by a laser-induced breakdown (LIB) spark is used as the density disturbance. This type of disturbance provides a nearly spherically symmetric shockwave flow that has been used previously to assess the response and position of multiple FLDI beams [3] or the uncertainty associated with FLDI-based velocity measurements [16, 17, 19]. A 1-dimensional, spherically symmetric CFD solution of this flow has been computed and is used as the input to the FLDI instrument simulations. Prior to performing instrument simulations, the CFD solution is compared quantitatively against results reported by Yan et al. [20] as well as qualitatively against experimental high-speed schlieren images obtained in this work for validation. The response of two FLDI instruments are then simulated. The first simulation is that of a two-point version of the conventional spherically-focusing FLDI as described in Refs. [16, 17]. The second simulation is that of a multi-point line FLDI instrument described in [19, 21] where focusing occurs in one direction while the laser light remains collimated in the orthogonal direction. The time-varying signals obtained from the simulated FLDI instruments are then compared against

signals obtained from experiment. A discussion of differences in the response of the two instrument configurations is then provided.

III. Experimental Setup

A. Two-Point FLDI Instrument

Figure 1 shows a schematic of the two-point FLDI system. Detailed information pertaining to this setup can be found in Refs. [16, 17]. In this system, the laser's center wavelength, λ_0, was 532 nm, the initial beam diameter was 0.7 mm, and the beam was linearly polarized. Two mirrors, M^{1P} and M^{2P}, directed the beam onto the instrument's optical axis. A half-wave plate HWP^{1P} and polarizing beam splitter (PBS) were used to control the laser power transmitted into the full instrument with vertical polarization, with the remainder directed into a beam dump, BD. A second half-wave plate, HWP^{2P}, then rotated the polarization angle to $45°$ with respect to the fast axis of the Nomarski prism, NP. Prior to the NP, a short focal length lens, BE, was used to expand the beam about the instrument's optical axis. A third half-wave plate, HWP^{3P}, rotated the polarization angle of the two beams exiting the NP by $\pm 45°$. A Wollaston prism, W^P, further split the beams into two additional beams. A field lens, FL^P, consisting of two achromat lenses, FL^{1P} and FL^{2P}, focused the diverging beams to a point in the test section corresponding to the instrument's measurement plane, denoted by section A-A. At the measurement plane the resulting Nomarski and Wollaston pair separation was $\Delta x_{NP} = 2431 \ \mu m$ and $\Delta x_{WP} = 257 \ \mu m$, respectively. The waist radius of each beam was $w_0 \approx 26 \ \mu m$ at their focus. Measurements of Δx_{NP}, Δx_{WP}, and w_0 were obtained by imaging the intensity distribution of the focused laser light at the measurement plane with a small CMOS camera. A Gaussian fit to each focused beam was used to estimate the waist radius and identify each beam's center location within this plane.
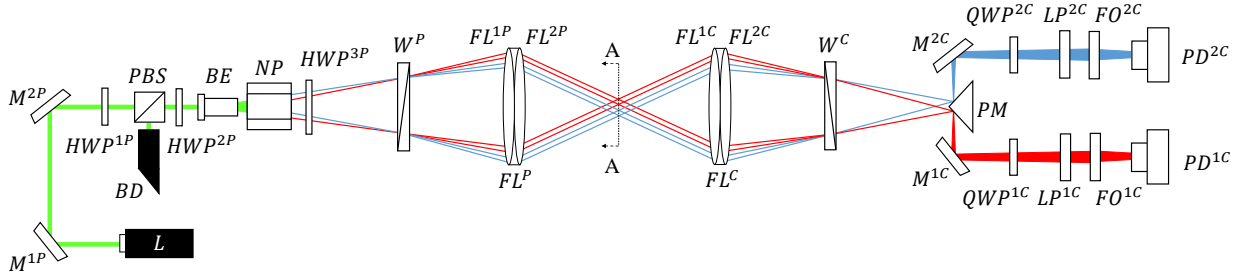

Fig. 1   Schematic of the optical setup for the two-point FLDI instrument.

On the catch side, the field lens, FL^C, and Wollaston prism, W^C, arrangement mirrored that of the pitch-side about the measurement plane. A knife-edge right-angle prism mirror, PM, was used to redirect light from each Wollaston pair in opposite directions. These beams were then directed into separate quarter-wave plates, QWP^{1C} and QWP^{2C}, by mirrors M^{1C} and M^{2C}, respectively, to remove ellipticity. Separate linear polarizers, LP^{1C} and LP^{2C}, were subsequently used to pass the polarization component corresponding to a phase offset of $\Delta \phi_{WP} = \pi/2$ between each Wollaston pair beam when no disturbances were present. Finally, focusing optics, FO^{1C} and FO^{2C}, were used to loosely focus each beam onto photodiode detectors, PD^{1C} and PD^{2C}, respectively. The output voltages of each photodiode were recorded at 250 MHz during the experiment using a digital oscilloscope with 50 Ω termination.

As previously mentioned, the Nomarski and Wollaston pairs were oriented vertically on the measurement plane (section A-A in Fig. 1) as shown in Fig. 2. For the two-point FLDI measurements, a tightly-focused 532 nm pulsed laser beam was used to generate a laser-induced breakdown (LIB) spark at a point $x = 66.7$ mm above the two-point FLDI instrument's optical axis and aligned to both the Nomarski and Wollaston pair separation axes. The resulting shockwave from the LIB spark traveled parallel to the separation axes of the beam pairs as shown in Fig. 2.

B. Multi-Point Line FLDI Instrument

The multi-point line FLDI instrument had an optical setup that was essentially identical to that of the two-point FLDI instrument with the exception of a few key optical component additions. In this version of the instrument, a series
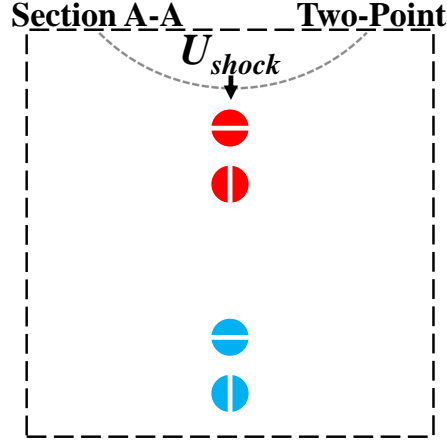
U_{shock}

Fig. 2 Two-point FLDI laser light orientation on measurement plane. White lines represent linear polarization orientation.

of cylindrical lenses were inserted at various positions along the instrument's optical axis so that lines of focused laser light (λ_0 = 532 nm) were formed parallel to the vertical axis (here the x-axis) on the measurement plane. Details pertaining to the setup of this system can be found in Ref. [19]. In this system, a positive cylindrical lens, PCL^P, was placed so that it collimated the beams with respect to the vertical direction while allowing them to continue to expand in the horizontal direction. In Fig. 3, the magenta color is used hereafter to describe the propagation of the laser beams when viewed from the side. A negative cylindrical lens, NCL^P, was then placed one focal length from W^P to further expand the beam in the vertical direction. A field lens, FL^P, consisting of two achromat lenses, FL^{1P} and FL^{2P}, was used to focus the beams in the horizontal plane and collimate them in the vertical plane. Using this configuration, the two line pairs (or Wollaston pairs) were formed on the measurement plane (section A-A) as shown in Fig. 4. Here, each line within each Wollaston pair is overlapped and aligned to the vertical axis, which is parallel to the direction of travel of the LIB shockwave. At the measurement plane the resulting Wollaston pair separation was Δx_{WP} = 173 μm. The focused lines were best represented by an ellipse with a major axis radius of $w_{major,0}$ = 4760 μm and minor axis radius of $w_{minor,0}$ =10 μm. Here it is important to note that the length of the lines, ΔL, can be specified with careful selection of BE, PCL^P, and NCL^P focal lengths.
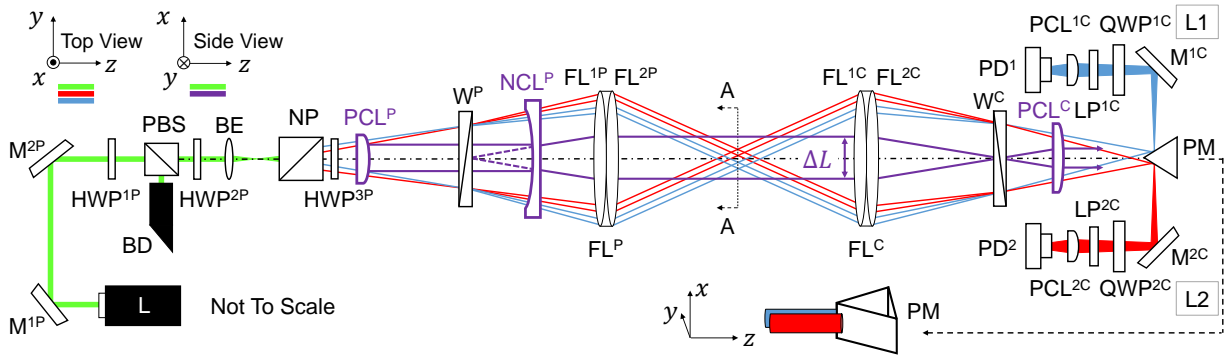
Fig. 3 Schematic of the optical setup for the two-line/multi-point FLDI instrument. Note that the x and y axes have been switched relative to the coordinate system notation used in Ref. [19]

.

Beyond the measurement plane (section A-A) in Fig. 3, light from the laser lines diverged in the horizontal direction and remained collimated in the vertical direction. As with the two-point system in Fig. 1, a second field lens, FL^C, and Wollaston prism, W^C, mirrored the setup on the pitch side of the instrument. The location of W^C also corresponded to the focus of the laser light in the vertical direction. After passing through W^C, the laser light began to diverge in the vertical direction. This light was then collimated in the vertical direction by placing a positive cylindrical lens, PCL^C,

one focal length from W^C. Beyond PCL^C the laser light from the Nomarski pair continued to converge in the horizontal direction until two focused laser lines were formed. The light from these lines was then directed into separate legs, L1 and L2, of the instrument by a right-angle prism mirror, PM, each containing identical optical components. An isometric view of this splitting of the two laser lines with PM can be seen at the bottom right of the schematic in Fig. 3. After reflection from a turning mirror, $M^{\#C}$, the beams passed through a quarter-wave plate, $QWP^{\#C}$, used to remove any polarization ellipticity. A linear polarizer, $LP^{\#C}$, then transmitted the component of polarization corresponding to the middle of the interference fringe and a short focal length positive cylindrical lens, $PCL^{\#C}$, was used to adjust the thickness of the laser line incident on the linear silicon PIN photodiode array, $PD^{\#}$. Selection of the focal length of PCL^C determined the length of the laser line incident on $PD^{\#}$. For the experiments described in this work, a 16-element silicon PIN photodiode array was used to record the interference pattern along the laser lines, with each element measuring 0.8 mm high (active height of h_{CH} = 0.7 mm) for a total height of 12.8 mm and a total width of 2.0 mm.
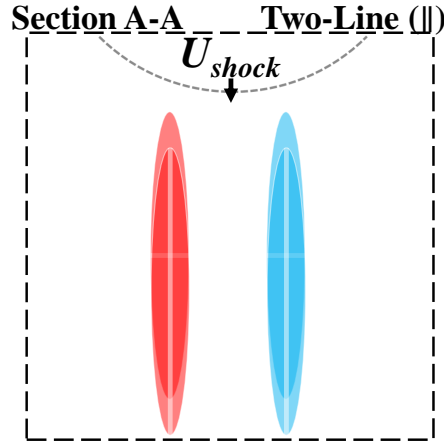

Fig. 4   Multi-point line FLDI configuration on measurement plane.

The time-varying current signals from the photodetector elements were terminated at 50 Ω and simultaneously digitized at 14-bit resolution using two 8-channel high-speed oscilloscope modules with the receipt of an external trigger pulse. Data were acquired at 50 MHz on each channel. Note that for this configuration, only a single line of measurement was obtained that was centered x = 53.2 mm below the LIB spark.

C. High-Speed Schlieren Imaging

For all experiments, a high-speed schlieren imaging system was oriented orthogonal to the FLDI instrument's optical axis as shown in Fig. 5, where a pulsed green LED was used as the schlieren light source. Figures 5a and 5b show a top and side view schematic of the schlieren imaging system setup, respectively. The left schematics in Fig. 5 show how the laser light is focused for the two-point FLDI instrument, represented by the red and blue lines, relative to the schlieren field-of-view (FOV). This is the configuration shown in Fig. 2. The right schematics in Fig. 5 show how the laser light is focused for the multi-point line FLDI configuration relative to the schlieren FOV. This setup corresponds to the configuration shown in Fig. 4. In this work, the schlieren images were used to visualize the shockwave and trailing expansion region resulting from the spark as they passed through the FLDI instrument's measurement plane. For the two-point FLDI measurements, a framing rate of 200 kHz was used, while for the multi-point line FLDI measurements, a framing rate of 400 kHz was used. For all experiments, the knife-edge of the schlieren system was placed parallel to the front surface of the shockwave. The FLDI data acquisition system also recorded a synchronization signal from the camera for comparison of the relative schlieren signal intensities to the relative FLDI signal intensities from each Wollaston pair.
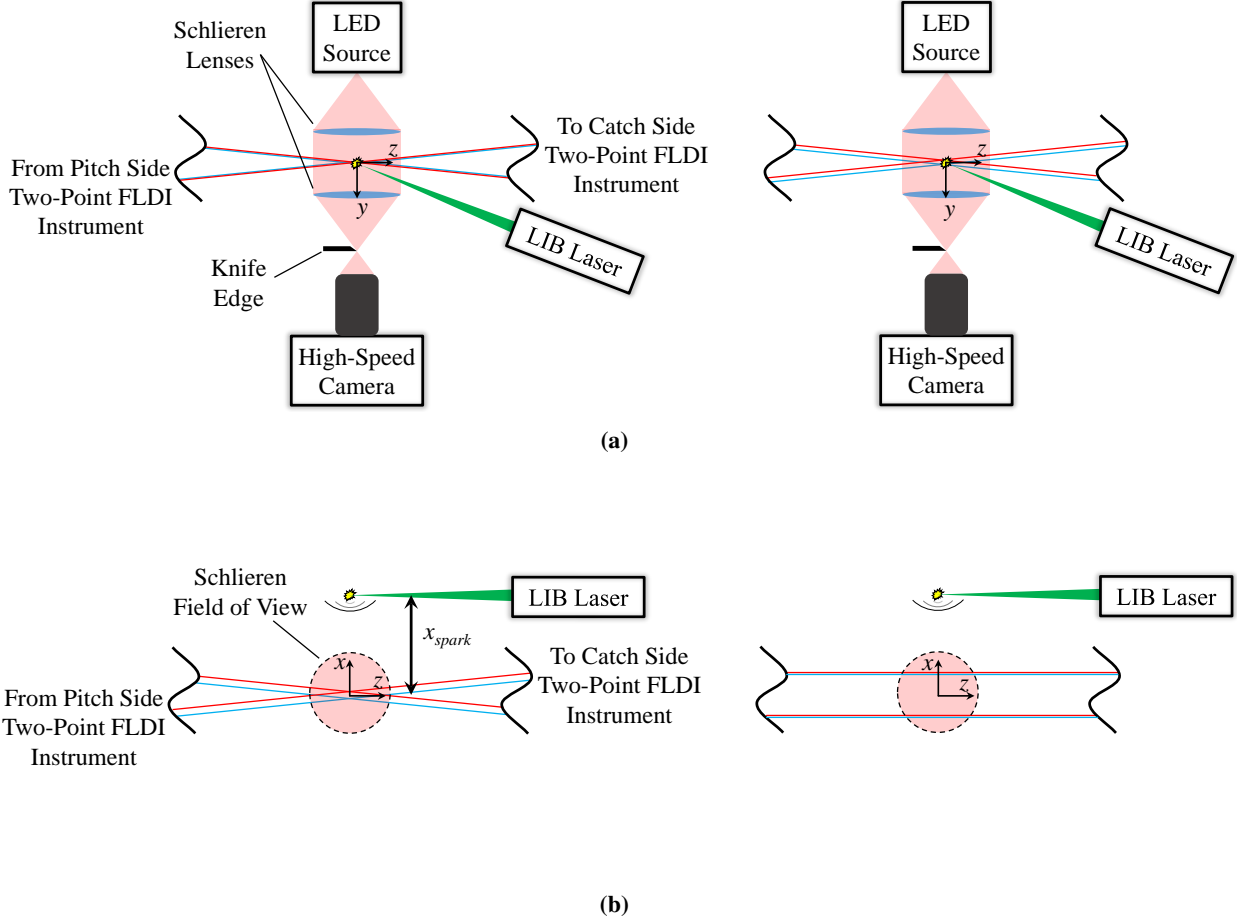
Fig. 5 (a) Top and (b) side views of high-speed schlieren imaging setup for (left) two-point [Fig. 2] and (right) multi-point line [Fig. 4] FLDI instrument configurations.

IV. Numerical Simulation Details

A. Laser-Induced Breakdown Spark Shockwave Computations

Simulations of the shockwave resulting from an LIB spark were performed using the *rhoCentralFoam* solver in OpenFOAM [22]. *rhoCentralFoam* is a compressible, density-based solver that uses a Godunov-like Kurganov-Tadmor scheme, which is total variation diminishing [23]. The time derivatives were discretized using the Crank-Nicholson algorithm. For this work, the flowfield was assumed to be spherically symmetric so only a 1-dimensional grid was used for the simulation. The grid consisted of 40,000 cells uniformly distributed in the radial direction with a cell size of 5 μm, giving an overall domain radius of r_e = 200 mm. A constant specific heat of C_p = 1005 kJ/(kg·K) and constant viscosity of μ = 1.81×10^{-5} Pa·s were assumed. The pressure and temperature were initially set to 101,325 Pa and 293 K throughout the domain.

Deposition of thermal energy from the laser spark was handled in a manner similar to that outlined Yan *et al.* [20]. To avoid singularity in the numerical solution, a small spherical sector of radius r_c = 30 μm was cut and removed from the computational domain. A zero-gradient boundary condition at the inlet and outlet face of the domain and wedge/axisymmetric boundary conditions along the side faces of the domain were also specified. Figure 6 shows a notional schematic of the computational domain. An initial temperature jump specified at the inlet was defined according to:

$$\Delta T_0 = \frac{\varepsilon E}{\pi^{\frac{3}{2}} r_0^3 \rho_\infty C_v} \tag{1}$$

where ΔT_0 is the temperature jump, ε the fraction of deposited laser energy absorbed by the air, E the deposited laser energy, r_0 the focused laser spot waist radius, ρ_∞ the ambient density, and C_v the specific heat at constant volume. For the FLDI instrument simulations, a laser energy of $E = 175$ mJ was used to compute the temperature jump and was based on the difference of 100 measurements of the laser energy obtained before and after the spark. A value of $\varepsilon = 0.45$ was assumed for these simulations. The spark radius, $r_0 = 900 \ \mu$m, was assumed to be the same as that in Ref. [20].
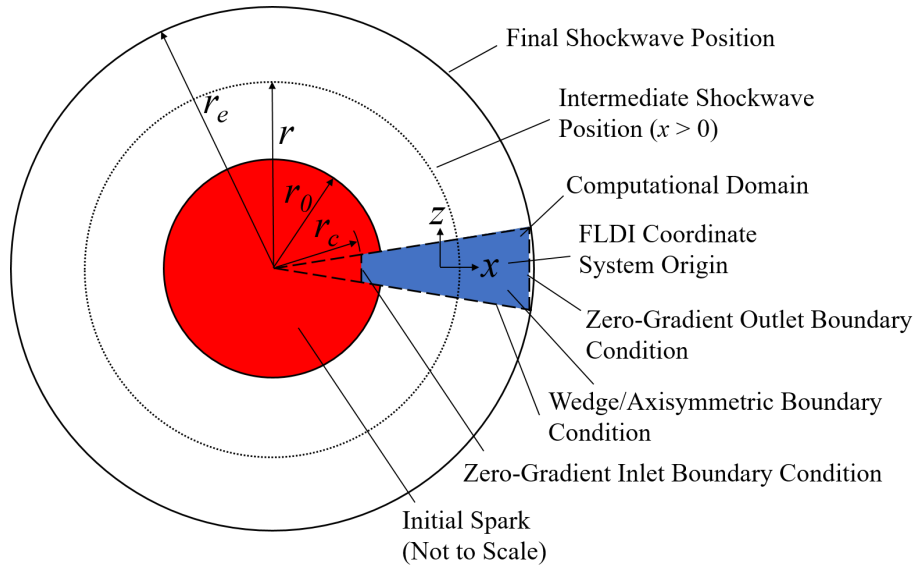
Fig. 6   Schematic of computational domain used for laser spark flow computations (not to scale). Here, the laser spark radius, r_0, is greatly exaggerated for clarity.

A grid convergence study was performed to ensure independence of the solution on the grid spacing. Computations were performed with cell sizes of 2.5 μm, 5.0 μm, and 10.0 μm. Results from this study are shown in Fig. 7. The resulting shockwave Mach number, M_s, as function of time (Fig. 7a) and normalized pressure profiles, p/p_∞, as functions of normalized radius, r/r_0, at several time steps (Fig. 7b) were then compared against one another. These results showed no significant differences between one another.

Another study was performed to ensure that the specified cut radius, r_c, had no influence on the laser spark simulation results. For this study, cut radii of 30 μm, 60 μm, and 90 μm were simulated. Results from this study are shown in Fig. 8. Again, profiles of M_s as a function of time (Fig. 8a) and p/p_∞ as a function of r/r_0 at several time steps (Fig. 8b) were compared against one another to ensure the solution was independent of r_c.

To quantitatively validate the laser spark simulation results obtained in this work, the normalized density profile, ρ/ρ_∞, as a function of normalized radius, r/r_0, for a laser pulse energy of $E = 145$ mJ and an absorption factor of $\varepsilon = 0.50$ was compared against both experimental and simulation results reported by Yan *et al*. [20] at $t = 20 \ \mu$s after the initial laser spark. Figure 9 shows that the CFD results obtained in this study exhibit relatively good agreement with simulations in [20] and closely match their experimental results. Also plotted in this figure is the density ratio profile for $E = 175$ mJ and $\varepsilon = 0.45$ used in instrument simulations for in this work, which closely matches the other simulation results. The only notable difference in the CFD simulations in this work from that reported in [20] occurs in the expansion region behind the shockwave between $5 < r/r_0 < 8$, where the density ratio computed in this study is slightly higher.

Qualitative validation of the laser spark simulation results was obtained by comparing the simulated density to a high-speed schlieren image sequence acquired during experiments performed with the two-point FLDI instrument configuration. Figure 10 shows this comparison beginning at $t \approx 147 \ \mu$s after the initial laser spark in 5 μs time increments. Here, the results from the numerical simulation are shown on the left ($z \leq 0$) and the experimental schlieren images on the right ($z > 0$). Scattered light from each Wollaston pair of the two-point FLDI instrument is shown in green false-color in each image. This scattered light was generated by spraying canned air near the focus of the instrument, which was then imaged by the high-speed schlieren camera when no laser spark shockwave was present. It
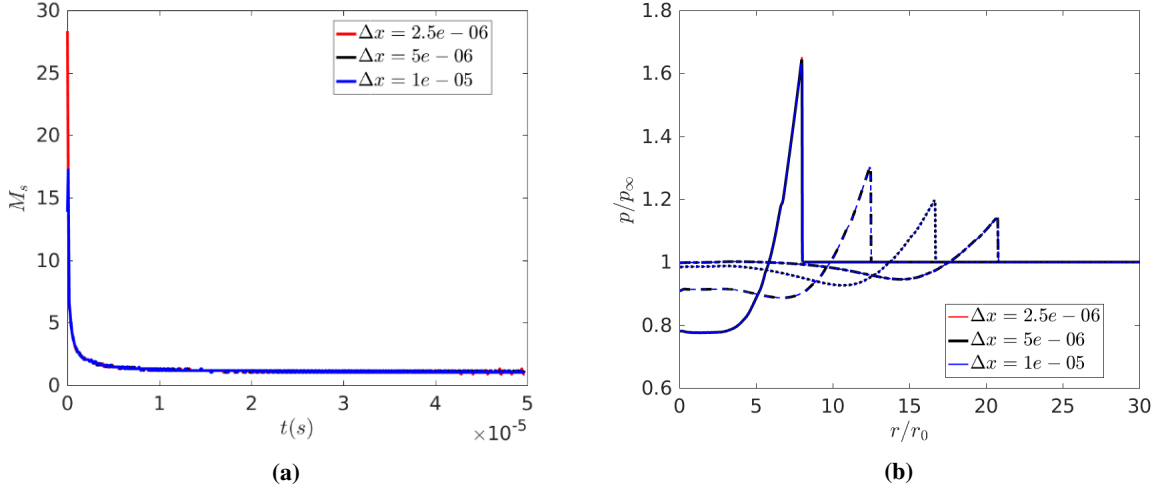
Fig. 7   Results of grid convergence study for cell sizes of 2.5, 5, and 10 μm. Results of (a) shockwave Mach number as a function of time and (b) pressure ratio as a function of normalized radius for several time steps for each cell size.
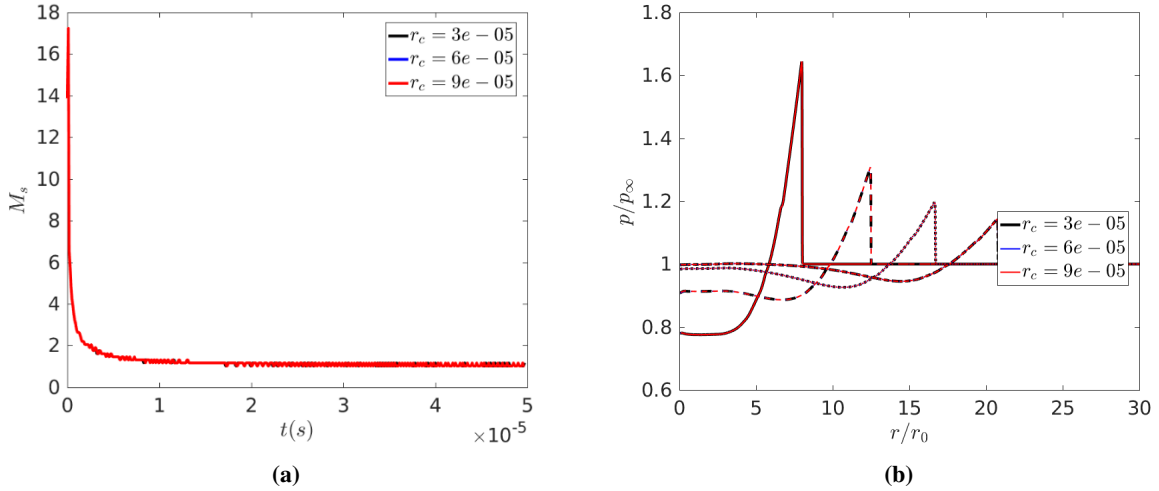

Fig. 8   Results of grid dependence study for cut radii of 30, 60, and 90 μm. Results of (a) shockwave Mach number as a function of time and (b) pressure ratio as a function of normalized radius for several time steps for each cut radius value.

should be noted that the simulation results represent the density field while the schlieren images are representative of the path-averaged vertical density gradient field. These images show that the numerical simulations accurately capture the propagation speed and location of the shockwave generated by the laser spark.

B. FLDI Instrument Simulation

To simulate the response of the two-point FLDI instrument, polar grids identical to those specified by Schmidt and Shepherd [18] are used that are evenly spaced in $\Delta z = 100\,\mu$m increments along the optical axis of each beam. As described in the previous section, density profiles, ρ, obtained from the CFD solution were used to compute the corresponding refractive index value for air, and then input into the FLDI instrument simulation at each grid point as described in this section. The output of this FLDI instrument simulation was then used to compare against experimental
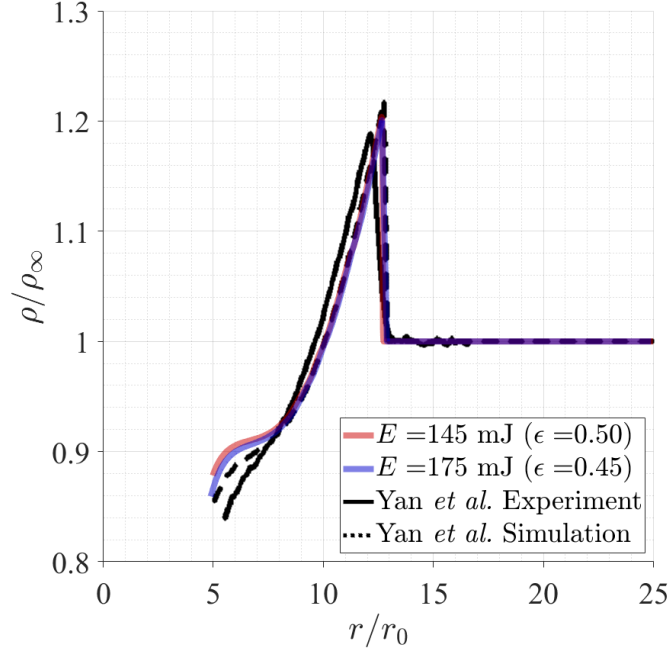
8

Fig. 9 Comparison of laser spark simulation results with work in Ref. [20] at $t = 20\ \mu$s.

FLDI signals. An example of the polar grid is shown in Fig. 11a at the measurement plane. As in Ref. [18], the polar grids extend to twice the local Gaussian beam waist radius, with radial grid points spaced from the outermost radial point according to:

$$r_k = r_{k-1}\left(\frac{2-\delta\theta}{2+\delta\theta}\right) \tag{2}$$

where $r_1 = 2w$, $r_{N-1} \approx w/1000$ (with a total number of N radially-spaced grid points), and $\delta\theta = 2\pi/300$ is the spacing of the grid in the azimuthal direction in units of radians. An additional grid point is placed at $r_N = 0$.

For the multi-point line FLDI simulation, a different gridding approach is used to ensure that the signal terminating on each simulated photodiode element in the linear array will include an equal number of grid points. Figure 11b shows a zoomed-in portion of the grid used to simulate the multi-point line FLDI instrument. Note here only every other grid point along the $\tilde{y}$ axis is plotted for clarity and that the full grid resembles a section an ellipse. For this grid, both minor ($w_{\text{minor},0} \approx 10\ \mu$m) and major ($w_{\text{major},0} \approx 4760\ \mu$m) waist radii are specified as the actual focused lines are best represented by an ellipse. Here, the grid spacing along the major axis is kept constant according to:

$$\Delta\tilde{x} = \frac{V}{400} \tag{3}$$

where V is the vertical height of each element on the linear photodiode array projected onto the measurement plane (section A-A in Fig. 3). For the experiment and simulation presented in this work, $V = 526\ \mu$m. With a total of $N_e = 16$ elements, a total of 6400 grid points were used in the $\tilde{x}$-direction. Using the equation for an ellipse, the outermost grid point at each $\tilde{x}$ point along the major axis of the line is:

$$\pm\tilde{y}_1 = 2w_{\text{minor}}\sqrt{1-\left(\frac{\tilde{x}}{2w_{\text{major},0}}\right)^2} \tag{4}$$

where w_{minor} is the minor axis width as a function of z. Finally, the inner grid spacing at each $\tilde{x}$ point along the major axis is defined as the intersection of successively smaller ellipses with minor axes specified as:

$$\tilde{y}_k = \tilde{y}_{k-1}\left(\frac{8-\frac{\Delta\tilde{x}}{2w_{\text{minor},0}}}{8+\frac{\Delta\tilde{x}}{2w_{\text{minor},0}}}\right) \tag{5}$$
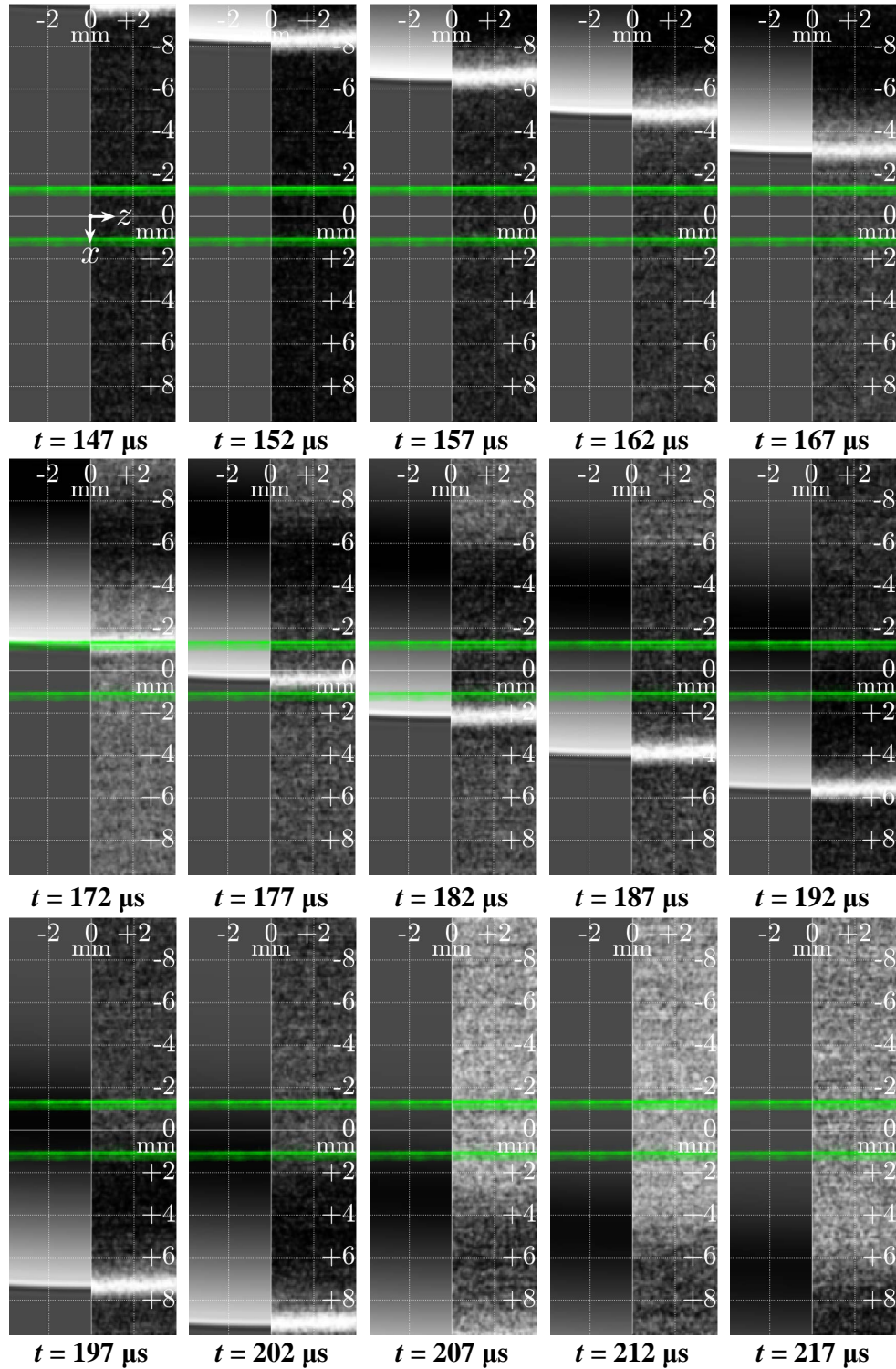
9

CFD   Schlieren

Fig. 10   Comparison of computed density field at $z = 0$ **for** $E = 175$ **mJ,** $\varepsilon = 0.45$ **(left) with high-speed schlieren images obtained with a horizontal knife edge (right) at several time steps beginning at** $t \approx 147$ μs **after the initial laser spark. Focused laser light from two-point FLDI instrument shown in green false color.**
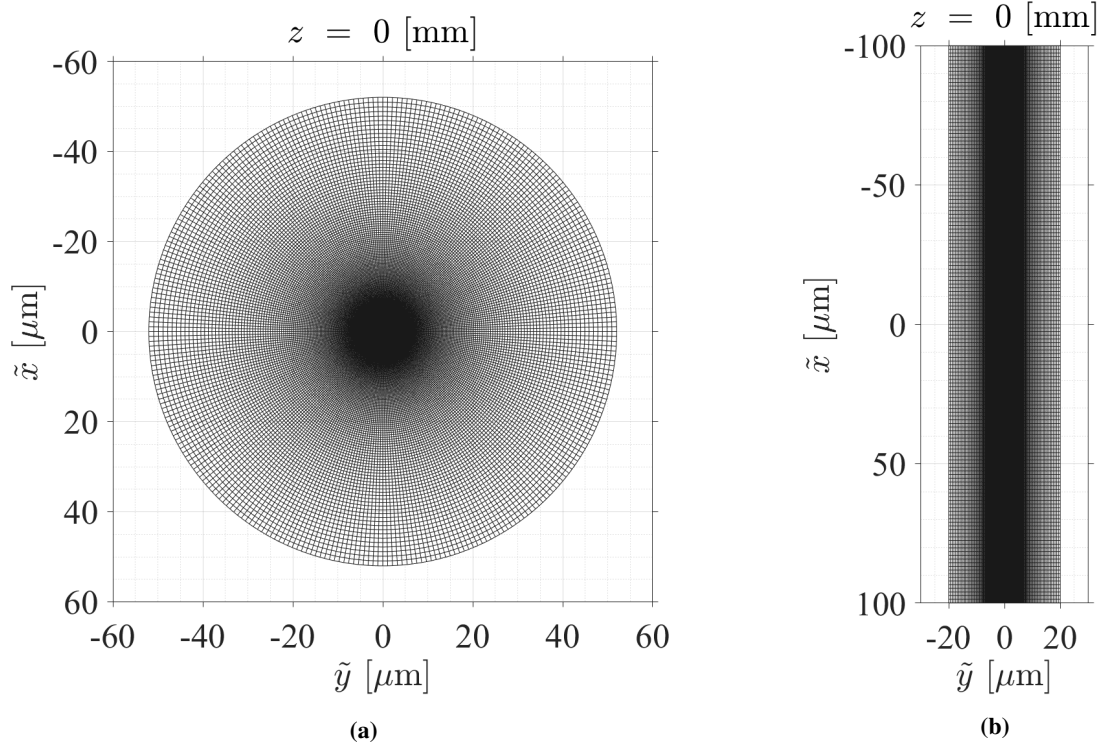
Fig. 11   Cross-sectional view of (a) two-point and (b) multi-point line FLDI simulation grids at $z = 0$.

The top-left image in Fig. 12 shows the placement of two-point FLDI simulation grids along the instrument's optical axis. Note that the spacing shown here is only notional and does not reflect the true grid spacing ($\Delta z = 100 \ \mu$m) that was used to simulate the two-point FLDI instrument. The remaining images in Fig. 12 show results from the numerical simulation of the shockwave beginning at $t = 172 \ \mu$s after the initial laser spark in 10 μs time steps (up to 232 μs). In these images, both the schlieren FOV plane (xz plane at $y = 0$) and those co-planar to the FLDI simulation grids (xy planes) are shown. As in the FLDI instrument simulations, the CFD data have been interpolated onto FLDI grids using a spline interpolation method. These figures best demonstrate why the shockwave flow from a laser spark was selected to assess the amplitude response of the two-point and multi-point line FLDI instruments. As the shockwave front propagates away from the FLDI instrument's focus, the gradient in density near the focus aligned to the Wollaston pair separation axis tends towards zero. As a result, the phase difference between the two Wollaston beams near the focus tends towards zero, and the contribution of the flowfield in this region to the FLDI signal becomes negligible. However, as the shockwave continues to propagate radially, significant gradients in density pass through the FLDI beams away from their focus. This provides a means to determine instrument sensitivity away from the instrument's focus.

V. Results

A. Two-Point FLDI Instrument Simulation

Figure 13 shows the signals obtained from the two-point FLDI instrument compared to the simulated FLDI instrument response. Here, the thick red and blue curves correspond to the experimental upstream (US) and downstream (DS) Wollaston pair signals obtained from the locations shown in Fig. 2. In Fig. 13a, simulations performed with Gaussian waist radii of w_0 of 2.5 μm, 5.0 μm, and 10.0 μm are compared with the experimental two-point FLDI signals. Fig. 13b shows a similar comparison, but with simulated w_0 values of 25.0 μm, 50.0 μm, and 100.0 μm. Note that the CFD data input to the FLDI simulation assumed a laser spark with $E = 175$ mJ and $\varepsilon = 0.45$. In these figures, the data have been normalized by the difference between maximum and minimum signal values observed in the upstream Wollaston pair for each case.
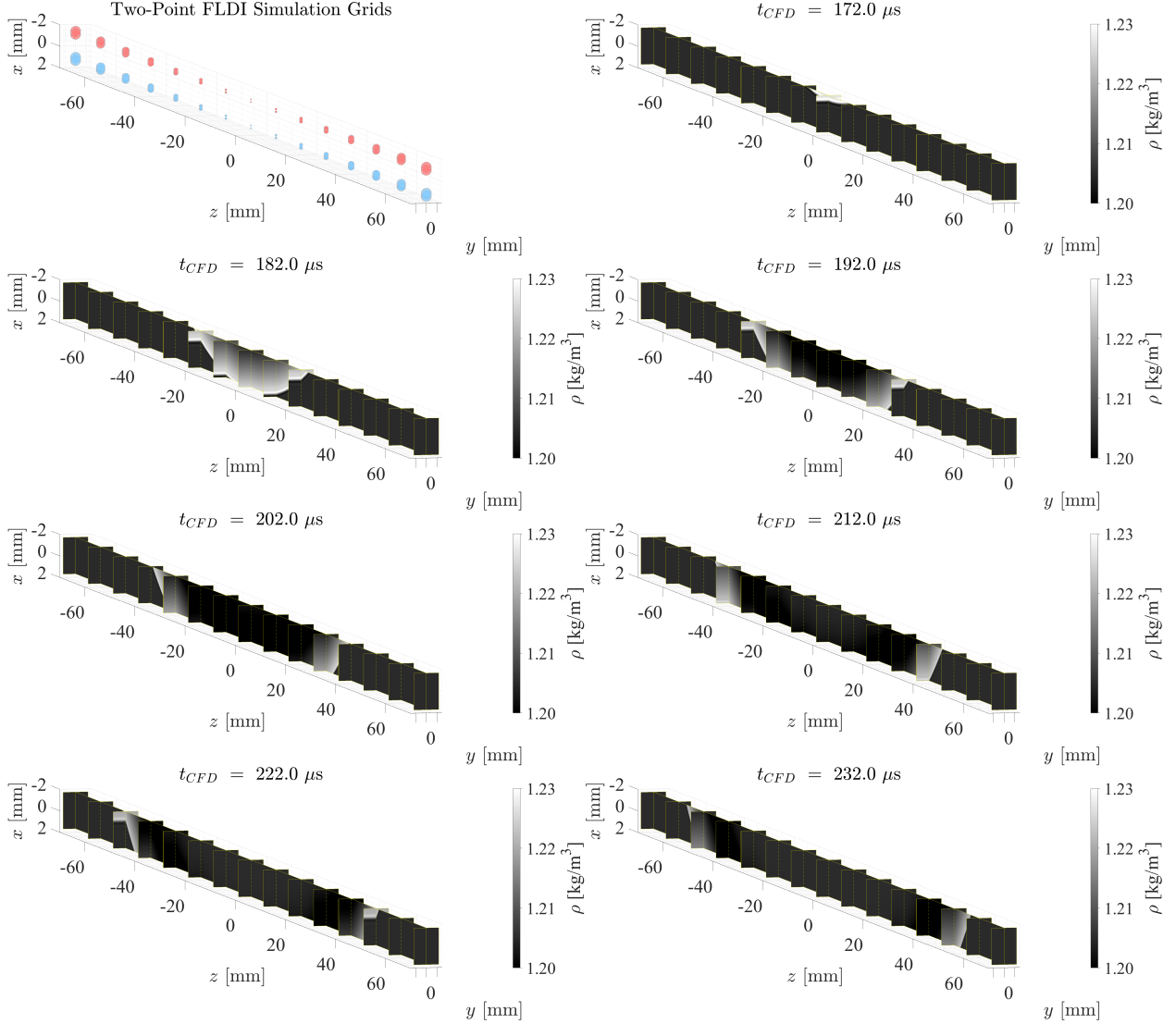
Fig. 12   Notional FLDI simulation grid shown in top-left image with CFD shockwave simulation results for $E = 175$ mJ, $\varepsilon = 0.45$ beginning 172 μs after intial laser spark shown in 10 μs time increments.

In Fig. 13a, the $w_0 = 2.5$ μm FLDI simulation provides the best match to the experimental two-point FLDI measurements in terms of normalized peak signal amplitude, normalized minimum signal amplitude (corresponding to the post-shock expansion region), and overall response. In this figure, however, it appears that decreasing w_0 in the instrument simulation results in an increasing signal rise time as the initial shockwave passes through the Wollaston pair when compared to the experimental data. In all cases, the simulated signals also exhibit a shorter fall time immediately after the initial shockwave passes when compared to the experimental data, and the point at which the simulated signals attain their minimum value occurs before the same point in the experimental signals. As w_0 is increased beyond 10.0 μm, as shown in Fig. 13b, no significant change in the simulated response of the instrument occurs aside from a small decrease in absolute signal magnitudes. While the simulated FLDI signals follow the general trends of the experimental data, the simulated signal appears to lead the experimental signal in time. As stated in Sec. III.A and reported in Refs. [16, 17], the experimental two-point FLDI instrument waist radius was measured to be $w_0 = 26$ μm. While, the simulated instrument response in Fig. 13b for $w_0 = 25$ μm most closely matches the conditions of the experiment, it fails to capture the character of expansion region immediately behind the shockwave. Note that the Wollaston pair spacing in these simulations has been kept constant at $\Delta x_{\text{WP}} = 257$ μm. Future work in which calculations where a sweep of Δx_{WP} values are simulated above and below the experimentally-measured value will be performed to determine
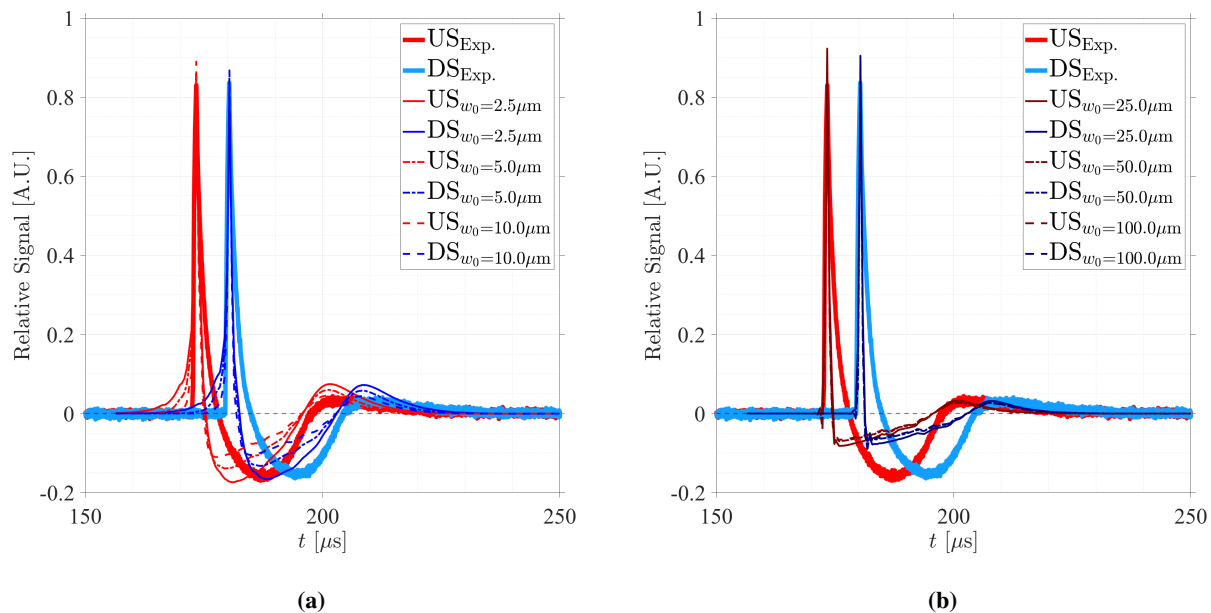
Fig. 13   Comparison of experimental two-point FLDI signals with simulated two-point FLDI system response for Gaussian waist radius values of (a) 2.5 μm, 5.0 μm, and 10.0 μm and (b) 25.0 μm, 50.0 μm, and 100.0 μm.

how it affects the response. As was performed in Ref. [18], future work will also include a grid convergence study for the simulated instrument response to ensure grid independence. Finally, and as will be discussed in the following section, future work will include a study on the influence of laser energy, E, and absorption coefficient, ε, on the CFD simulation and resulting simulated instrument response.

B. Multi-Point Line FLDI Instrument Simulation

Figure 14a shows the experimental signals obtained from the multi-point line FLDI instrument as shown schematically in Fig. 3. Here, only measurements from a single line using a 16-element photodiode array in the configuration shown in Fig. 4 are presented. The darker curves in this figure correspond to measurements made closer to the initial laser spark. As the shockwave travels through the focused laser line, the downstream photodiode elements begin to register signal from the shockwave. The variation in peak amplitude registered on each element demonstrates the Gaussian intensity distribution of the light along the major axis of the focused laser line. Note here that the general amplitude response of the experimental signals obtained with the multi-point line FLDI instrument in this configuration differs somewhat from that of the spherically-focused experimental signals shown in Fig. 13. This is a consequence of the means by which the laser light is focused onto the measurement plane. For the multi-point line FLDI instrument, light is focused only in the *y*-direction (Fig. 3) altering its ability to reject the contributions of flow structures away from the focus relative to the spherically-focused instrument (Fig. 1). Figure 14b shows the simulated instrument response (circle symbols) at each channel (denoted on the vertical axis) compared to the experimental data (solid lines) presented in Fig. 14a. In this figure, the shockwave propagates downward through each channel and is first registered on channel 1, with each subsequent channel registering a peak signal at later times. Here, the simulated instrument response compares favorably against the experimental data with respect to the predicted peak signal amplitude and time at which the peak signal amplitude occurs in time for each of the 16 channels. Beyond this, however, the general characteristics of the experimental data, such as the dip in signal prior to arrival of the shockwave or the positive amplitude post-shock region, are not captured as accurately by the instrument simulation.

Figure 15a provides a more detailed view of a comparison between the normalized experimental and simulated instrument signals as a function of time for channel 6 shown previously in Fig. 14b. Note that the small-scale repetitive disturbances within the experimental signal (for instance at 151 μs) is a result of RF interference from a pulsed LED
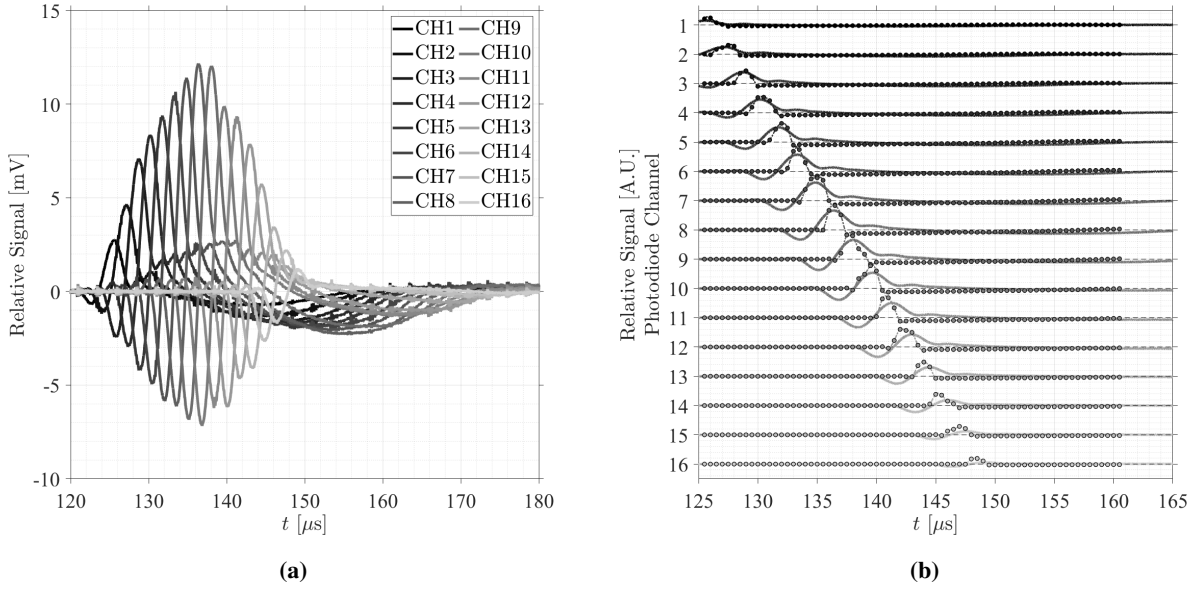
Fig. 14 (a) Experimental signals from 16 channels along a single line from the multi-point line FLDI instrument and (b) comparison of simulated instrument response (points with lines) to these experimental signals (solid lines).

used in simultaneous schlieren measurements described in Ref. [19] and do not significantly affect the measurement. While general similarities in the amplitude response between the experimental and simulated instrument response are observed, it is apparent that the simulated instrument response fails to capture several key features observed in the experimental signal. First, the amplitude and width in the initial dip that occurs in the experimental signal (with the minimum signal occurring at $t \approx 130.5~\mu$s) is much more pronounced and occurs 1.5 μs earlier than what is observed in the simulated response. Second, the relative peak amplitude and width of the shockwave signature are smaller and wider in the experiment compared to the simulation. Finally, the signal corresponding to the transition to the post-shock expansion region in the experimental data is much broader and exhibits an initially positive amplitude (between 135 μs $< t <$ 165 μs) compared to the simulated result.

After the preliminary comparison between the experimental and simulated multi-point line FLDI signals was performed, data from other laser spark experiments with this configuration were analyzed to determine if an experiment with a response similar to that predicted by the instrument simulation was observed. Figure 15b shows an experimental signal obtained during a laboratory test performed in December of 2019 that exhibited a relative response (black solid line) very closely matched to that predicted by the instrument simulation for channel 6 (green solid line with square symbols). In this figure, the time axis has been replaced by a spatial axis, $\tilde{x}'$, obtained by multiplying by the measured shockwave velocity reported in [17] of U_{shock} = 350.1 m/s. The peaks of each signal have then been shifted such that they occur at $\tilde{x}' = 0$. Here, the simulated signal from channel 6 (green line with square symbols), recast as a function of space, closely follows the experimental response of the instrument, with the most significant discrepancies occurring in the post-shock expansion region for $\tilde{x}' >$ 1.2 mm and in the signal troughs immediately before and after the peak amplitude signature of the shockwave. The solid red curve shown in Fig. 15b is the distribution of signal over the length of the simulated linear array element integrated only in the direction of the beam's minor axis. This signal exhibits better agreement with the experimental signal in terms of capturing the relative amplitudes of the troughs and peak signal. However, when the spatial axis of this simulated signal is scaled by the ratio of the true photodiode element height plus the Wollaston spacing, $h_{CH} + \Delta x_{WP}$, to the element height projected onto the measurement plane, V, the best agreement between experiment and simulation is obtained (red dashed line with circular symbols in Fig. 15b). This scaling is representative of the uncertainty that may be associated with V as measured with the knife-edge calibration method described in Ref. [19, 21].

The results presented in Fig. 15 show that the simulation method developed for the multi-point line FLDI instrument in this work is capable of capturing the response of the experimental instrument if the appropriate set of simulation
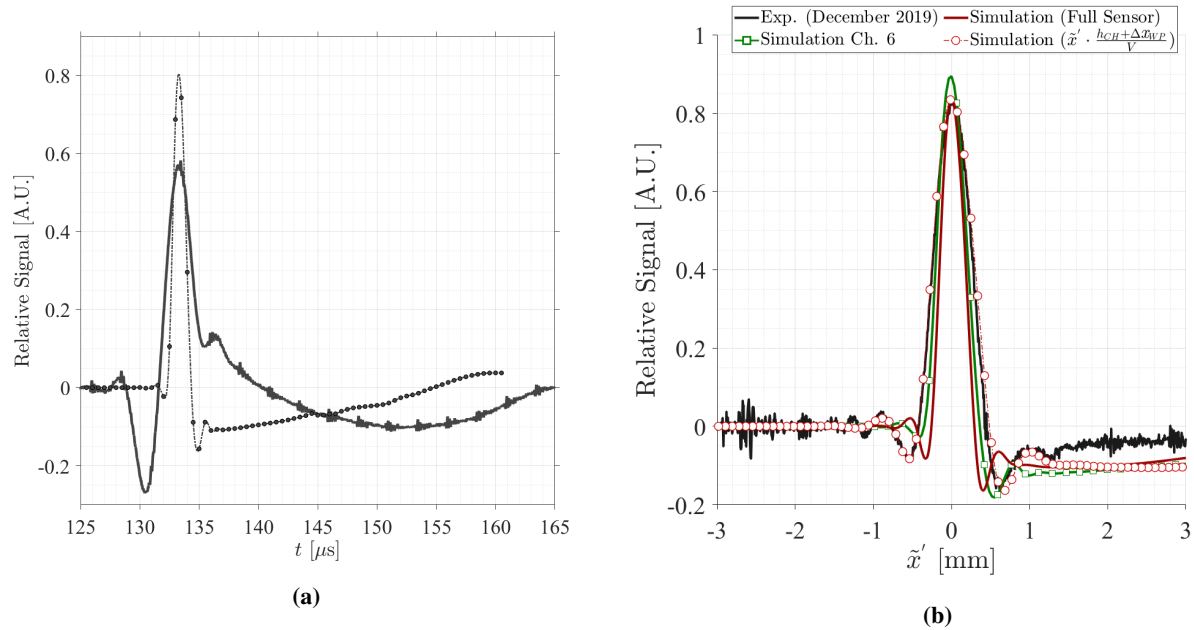
14

Fig. 15 **(a) Comparison of experimental (solid line) and simulated (dash-dot line with circular symbols) signals from a multi-point line FLDI instrument on channel 6 from Fig. 14b and (b) comparison of the simulated signal from channel 6 from Fig. 14b (solid green line with square symbols) and across the entire linear photodiode array (solid red line and dashed red line with circular symbols) with an experimental signal from an experimental performed in December 2019 recast in spatial coordinates.**

parameters are used. The agreement between experiment and simulation obtained in Fig. 15b is thought to be the result of a lower laser pulse energy and absorption factor, εE, used in the December 2019 experimental data that more closely matched that simulated in the CFD of this work. In this work, the value of $\varepsilon = 0.45$ was assumed, but may in fact be closer to unity for the data presented in Fig. 14a. Unfortunately, no measurement of laser energy was obtained for the December 2019 experimental data. Future work will include additional simulations with the multi-point line FLDI instrument using CFD with values of $\varepsilon > 0.45$ to address the role of laser energy absorption on the resulting shockwave flow and instrument response. As with the two-point FLDI simulation, a full grid convergence study will also need to be performed to ensure that the simulated multi-point line FLDI instrument response is independent of grid sizing.

VI. Conclusions

This paper presented simulated response data from two different FLDI instrument configurations when subjected to a shockwave flow generated by an LIB spark. The input to the instrument simulations consisted of a CFD simulation of the shockwave flow computed using the *rhoCentralFoam* solver in OpenFOAM that was quantitatively validated against previously published work and qualitatively validated against schlieren flow visualization images obtained in this work. For the two-point FLDI instrument simulation, general agreement in amplitude response between experiment and instrument simulation was observed. For the multi-point line FLDI instrument simulation, a general agreement in trends of peak amplitude and timing were observed between experiment and simulation. However, several parameters used in the shockwave flow and instrument simulations were identified that require additional study. Of primary interest will be the influence of varying projected photodiode element length scales onto the measurement plane (for the multi-point line FLDI instrument), Wollaston pair separation, and absorbed laser pulse energy.

15

Acknowledgments

References

[1] Smeets, G., and George, A., "Laser-Differential Interferometer Applications in Gas Dynamics," Tech. Rep. 28/73, Institut Franco-Allemand de Recherches Saint-Louis, 1973, Nov. 1973.

[2] Parziale, N., Shepherd, J., and Hornung, H., "Reflected Shock Tunnel Noise Measurement by Focused Differential Interferometry," *42nd AIAA Fluid Dynamics Conference and Exhibit*, American Institute of Aeronautics and Astronautics, 2012.

[3] Parziale, N. J., Shepherd, J. E., and Hornung, H. G., "Differential Interferometric Measurement of Instability at Two Points in a Hypervelocity Boundary Layer," *51st AIAA Aerospac Sciences Meeting Including the New Horizons Forum and Aerospace Exposition*, American Institute of Aeronautics and Astronautics, 2013.

[4] Parziale, N. J., Shepherd, J. E., and Hornung, H. G., "Differential Interferometric Measurement of Instability in a Hypervelocity Boundary Layer," *AIAA Journal*, Vol. 51, No. 3, 2013, pp. 750–754.

[5] Parziale, N., "Slender-Body Hypervelocity Boundary-Layer Instability," Ph.D. thesis, California Institute of Technology, 05 2013.

[6] Fulghum, M. R., "Turbulence Measurements in High-Speed Wind Tunnels Using Focusing Laser Differential Interferometry," Ph.D. thesis, The Pennsylvania State University, 12 2014.

[7] Parziale, N. J., Shepherd, J. E., and Hornung, H. G., "Free-stream density perturbations in a reflected-shock tunnel," *Experiments in Fluids*, Vol. 55, No. 2, 2014, p. 1665.

[8] Parziale, N. J., Jewell, J. S., Leyva, I. A., and Shepherd, J. E., "Effects of Shock-Tube Cleanliness on Slender-Body Hypersonic Instability and Transition Studies at High Enthalpy," *53rd AIAA Aerospace Sciences Meeting*, American Institute of Aeronautics and Astronautics, 2015.

[9] Parziale, N. J., Shepherd, J. E., and Hornung, H. G., "Observations of hypervelocity boundary-layer instability," *Journal of Fluid Mechanics*, Vol. 781, 2015, pp. 87–112.

[10] Jewell, J. S., Parziale, N. J., Lam, K.-Y., Hagen, B. J., and Kimmel, R. L., "Disturbance and Phase Speed Measurements for Shock Tubes and Hypersonic Boundary-Layer Instability," *32nd AIAA Aerodynamic Measurement Technology and Ground Testing Conference*, American Institute of Aeronautics and Astronautics, 2016.

[11] Settles, G. S., and Fulghum, M. R., "The Focusing Laser Differential Interferometer, an Instrument for Localized Turbulence Measurements in Refractive Flows," *Journal of Fluids Engineering*, Vol. 138, No. 10, 2016, pp. 101402–101402–10.

[12] Houpt, A., and Leonov, S., "Focused Laser Differential Interferometer for Supersonic Boundary Layer Measurements on Flat Plate Geometries," *AIAA Aviation Forum*, American Institute of Aeronautics and Astronautics, 2018.

[13] Chou, A., Leidy, A. N., Bathel, B. F., King, R. A., and Herring, G. C., "Measurements of Freestream Fluctuations in the NASA Langley 20-Inch Mach 6 Tunnel," *AIAA Aviation Forum*, American Institute of Aeronautics and Astronautics, 2018.

[14] Ceruzzi, A., and Cadou, C. P., "Simultaneous Velocity and Density Gradient Measurements using Two-Point Focused Laser Differential Interferometry," *AIAA Scitech 2019 Forum*, AIAA SciTech Forum, American Institute of Aeronautics and Astronautics, 2019.

[15] Houpt, A. W., and Leonov, S. B., "Focused and Cylindrical-Focused Laser Differential Interferometer Characterization of SBR-50 at Mach 2," *AIAA Aviation 2019 Forum*, American Institute of Aeronautics and Astronautics, 2019. https://doi.org/10.2514/6.2019-3383.

[16] Weisberger, J., Bathel, B. F., Jones, S. B., and Herring, G. C., "Focused Laser Differential Interferometry Measurements at NASA Langley 20-Inch Mach 6," *AIAA Aviation 2019 Forum*, American Institute of Aeronautics and Astronautics, 2019. https://doi.org/10.2514/6.2019-2903.

[17] Bathel, B. F., Weisberger, J. M., Herring, G. C., King, R. A., Jones, S. B., Kennedy, R. E., and Laurence, S. J., "Two-point, parallel-beam focused laser differential interferometry with a Nomarski prism," *Applied Optics*, Vol. 59, No. 2, 2020, p. 244. https://doi.org/10.1364/ao.59.000244.

[18] Schmidt, B. E., and Shepherd, J. E., "Analysis of focused laser differential interferometry," *Applied Optics*, Vol. 54, No. 28, 2015, pp. 8459–8472.

[19] Weisberger, J., Bathel, B., Herring, G., Buck, G., Jones, S., and Cavone, A., "Multi-Point Line Focused Laser Differential Interferometer for High-Speed Flow Fluctuation Measurements," *Applied Optics*, 2020. https://doi.org/10.1364/ao.411006.

[20] Yan, H., Adelgren, R., Boguszko, M., Elliott, G., and Knight, D., "Laser Energy Deposition in Quiescent Air," *AIAA Journal*, Vol. 41, No. 10, 2003, pp. 1988–1995. https://doi.org/10.2514/2.1888.

[21] Weisberger, J. M., Bathel, B. F., Herring, G. C., Buck, G. M., Jones, S. B., and Cavone, A. A., "Two-Line Focused Laser Differential Interferometry of a Flat Plate Boundary Layer at Mach 6," *2021 AIAA Scitech Forum*, American Institute of Aeronautics and Astronautics, 2021.

[22] *OpenFOAM v7 User Guide*, The OpenFOAM Foundation, https://cfd.direct/openfoam/user-guide, 2020.

[23] Greenshields, C. J., Weller, H. G., Gasparini, L., and Reese, J. M., "Implementation of semi-discrete, non-staggered central schemes in a colocated, polyhedral, finite volume framework, for high-speed viscous flows," *International Journal for Numerical Methods in Fluids*, 2009. https://doi.org/10.1002/fld.2069.